



Article

A New Possible Way to Detect Axion Antiquark Nuggets

Ionel Lazanu [†]  and Mihaela Parvu ^{*,†} 

Faculty of Physics, University of Bucharest, P.O. Box MG-11, 030018 Bucharest, Romania; ionel.lazanu@g.unibuc.ro

* Correspondence: mihaela.parvu@unibuc.ro

† These authors contributed equally to this work.

Abstract: The axion anti-quark nugget (AQN) model was developed to explain in a natural way the asymmetry between matter and antimatter in Universe. In this hypothesis, a similitude between the dark and the visible components exists. The lack of observability of any type of dark matter up to now, in particular AQNs, requires finding new ways of detecting these particles, if they exist. In spite of strong interaction with visible matter, for such objects a very small ratio of cross section to mass is expected and thus huge detector systems are necessary. This paper presents a new idea for the direct detection of the AQNs using minerals as natural rock deposits acting as paleo-detectors, where the latent signals of luminescence produced by interactions of AQNs are registered and can be identified as an increased and symmetrical deposited dose. The estimates were made for minerals widely distributed on Earth, for which the thermoluminescence (TL) signal is intense and if the thermal conditions are constant and with low temperatures, the lifetime of the latent signals is kept for geological time scales.

Keywords: dark matter; AQN; TL OSL dosimetry; minerals; detectors



Citation: Lazanu, I.; Parvu, M. A New Possible Way to Detect Axion Antiquark Nuggets. *Symmetry* **2024**, *16*, 869. <https://doi.org/10.3390/sym16070869>

Academic Editors: Antonia Di Crescenzo and Konstantin Zioutas

Received: 20 May 2024

Revised: 25 June 2024

Accepted: 5 July 2024

Published: 9 July 2024



Copyright: © 2024 by the authors. Licensee MDPI, Basel, Switzerland. This article is an open access article distributed under the terms and conditions of the Creative Commons Attribution (CC BY) license (<https://creativecommons.org/licenses/by/4.0/>).

1. Introduction

A large fraction of the matter in the Universe is not directly observable; its origin is not yet understood, and it is generically referred to as Dark Matter (DM). The existence of DM was established by observations from galactic to cosmological scales, where many phenomena can be better understood if the presence of additional (unobserved) matter is assumed. In order to understand what DM truly is, it is necessary to unambiguously observe its possible interactions with ordinary matter. Regarding the origins and characteristics of DM, a wide variety of particles have been predicted in different theories or phenomenologically, ranging from very massive macroscopic objects like primordial black holes and MACHOs to cold DM, warm DM, milli-charged particles, self-interacting DM, Weakly Interacting Slim Particles (WISPs), ultra-light (fuzzy) dark matter, or Weakly Interacting Massive Particles (WIMPs). Other examples are gravitinos, axions, neutralinos, strangelets, Q balls, and sterile neutrinos. For a more complete review, see [1]. There is a wide variety of experiments searching for axions, QCD axions, and axion-like particles. These include ADMX [2], CAST [3], ALPS [4], HAYSTAC [5], MADMAX [6], IAXO [7], and CASPER [8] experiments, each employing unique techniques to probe the existence of these elusive particles. Notable examples of experiments that are actively searching for WIMPs include the LUX [9] experiment, CDMS [10], SuperCDMS [11], the XENON1T [12] experiment, and the AMS-02 project [13].

Predicting the existence of axion (anti-)quark nuggets as exotic constituent particles of dark matter (DM) has a long history, beginning with the pioneering work of Witten [14] and De Rujula and Glashow [15] until their detailed definition proposed by Zhitnitsky [16]. DM and baryogenesis are two sides of the same coin; apparently, these two phenomena are uncorrelated. In fact, in the Big Bang model, the existence of axion quark nuggets and

axion antiquark nuggets can restore the symmetry between matter and antimatter if the total baryon numbers satisfy the following relations:

$$B_{\text{visible}} : B_{\text{nuggets}} : B_{\text{antinuggets}} \approx 1 : 2 : 3 \quad (1)$$

$$B_{\text{tot}} = 0 = B_{\text{nuggets}} - B_{\text{antinuggets}} + B_{\text{visible}} \quad (2)$$

Importantly, the basic available constraints from Big Bang nucleosynthesis (BBN) and the cosmic microwave background (CMB) are not in contradiction with the existence of this form of antimatter [17].

Oaknin and Zhitnitsky [18] proposed a novel scenario to explain the observed cosmological asymmetry between matter and antimatter, which relies on a mechanism of separation of quarks and antiquarks in two coexisting phases at the end of the cosmological QCD phase transition. Some fractions are bound into heavy nuggets of quark matter in a color superconducting phase. Nuggets of both matter and antimatter are formed as a result of the dynamics of the axion domain walls [16]. The observed difference between the quantities of nuggets (Ω_N) and antinuggets ($\Omega_{\bar{N}}$) generated by charge-parity (CP) violation unequivocally suggests that the baryon contribution (Ω_B) must be of the same order of magnitude as $\Omega_{\bar{N}}$ and Ω_N . This is because all these components are proportional to the fundamental dimensional parameter (Λ_{QCD}), as are all other dimensional parameters in QCD, such as the color superconducting (CS) gap (Δ), critical temperature (T_c), and chemical potential (μ). The remaining antibaryons in the plasma of the early universe were then annihilated, leaving only the baryons. The antimatter counterparts of these baryons are bound in the excess of antiquark nuggets and are, thus, unavailable for fast annihilation. Since all asymmetry effects are of order one, similarities arise among all components, both visible and dark. The observed ratio of matter to dark matter, $\Omega_{\text{DM}} \approx 5 \cdot \Omega_B$, implies a scenario where the baryon charge concealed in antinuggets exceeds that in nuggets by a factor of approximately ($\Omega_{\bar{N}}/\Omega_N$) $\approx 3/2$ at the end of nugget formation [19]. Recently, Sebastian Baum et al. proposed a systematic direction for the investigation of neutrino interactions and searches for exotic particles predicted in the extensions of the Standard Model or only phenomenological models using effects in different minerals and rocks [20].

Starting from the reference work by Polymeris et al. [21], the current article proposes the detection of axion antiquark nuggets in complex systems using the spatial distribution of the deposited doses in various minerals from natural deposits.

2. The Structure of the A \bar{Q} Ns and Their Interactions

Inside A(anti)QN, multiple regions with distinct structures and different length scales exist; for details, see [22,23]. In accordance with Gorham and Rotter [24] and Forbes and Zhitnitsky [25], these A \bar{Q} Ns carry a(n) (anti)baryon charge ($|B| \approx 10^3 \div 10^{33}$). These values of the baryon number are typically constrained by the expected dark matter (DM) flux and, thus, the A \bar{Q} N flux.

A \bar{Q} Ns made of antimatter are capable of releasing a significant amount of energy when they enter Earth's atmosphere and annihilation processes start to occur between antimatter hidden in the form of A \bar{Q} Ns and atmospheric or other materials such as rocks. In accordance with the equation for the energy loss derived by De Rujula and Glashow [15] and with the explicit form for the case of A \bar{Q} Ns,

$$-\frac{dE}{dx} = \begin{cases} \sigma_{\text{AQN}} \rho(x) v_{\text{AQN}}^2(L) & \text{if } v_{\text{AQN}}(L) \geq \sqrt{\frac{\varepsilon}{\rho}} \\ \varepsilon \sigma_{\text{AQN}} & \text{if } v_{\text{AQN}}(L) < \sqrt{\frac{\varepsilon}{\rho}}, \end{cases} \quad (3)$$

where σ_{AQN} is the cross section associated with the area of the nugget, and $\rho(x)$ is the density of the medium. For a well-defined distance (L),

$$v_{\text{AQN}}(L) = v_{\text{AQN}}(0) \exp\left(-\frac{\sigma_{\text{AQN}}}{M_{\text{AQN}}} \int_0^L \rho dx\right). \quad (4)$$

The equation of the energy loss breaks down at low velocity, when the force generated by the particle becomes equal to or lower than the force by which the material is confined. For velocities below $\sqrt{\varepsilon/\rho}$, the energy loss decreases at a constant rate and is brought to zero. The variation in the velocity of nuggets with distance can be expressed as $v_{AQN}(L)$, where for the cross section can be expressed by the geometric formulas $\sigma_{AQN} = \pi R_{AQN}^2$ and $R_{AQN} = 10^{-7} \left(\frac{B}{10^{24}} \right)^{1/3}$ [m].

AQNs are highly dense objects with a radius on the order of μm . Thus, when such an object travels through matter, the temperature should locally increase. In the lithosphere, the integrity of rocks persists up to an energy density of $\varepsilon = 6.2102 \text{ eV/cm}^3$. Because most major rocks and minerals have very similar densities, around 2.6 to 3.0 g/cm^3 , for velocities of nuggets below the value of 188 m/s , the energy loss is independent of their motion. At rest, nuggets accumulate in the Earth's crust and annihilate.

In the atmosphere, the parameters of interest vary strongly, depending on a multitude of factors. The atmospheric composition can be approximated considering only molecular nitrogen, which represents nearly 78% of the atmospheric concentration, and oxygen, accounting for 21%. Molecular nitrogen has a triple bond between the two atoms, one sigma bond, and two pi bonds. This bond is very strong and requires 941 kJ/mol of energy to break, compared to only 495 kJ/mol for molecular oxygen. Considering an average density for the atmosphere of around 0.657 kg/m^3 (as a mean value between sea level and an altitude of $2 \times 10^4 \text{ m}$), the energy loss is proportional with v^2 up to approximately 6.4 m/s . The average variations in air pressure, temperature, and density with altitude (the standard atmosphere and the mean values of the parameters) are available in [26].

Initially, an AQN is neutral electric. AQNs made of antimatter are capable of releasing a significant amount of energy when they enter the atmosphere and the Earth's crust. In accordance with [19], the binding energy of positrons is $E_{\text{bound}} \sim \text{keV}$. A large number of weakly bound positrons get excited and can leave the system. If an electric field is produced in the vicinity of an AQN through polarization effects, then positrons can be accelerated up to 10 MeV . As a result of these processes, the AQN acquires a negative electric charge and further ionizes the medium as a projectile with a mass of $M \approx m_p B$.

In the work cited above, Ariel Zhitnitski invoked arguments related to the emission by AQNs of axions and their expected characteristics. The total energy of an AQN finds its equilibrium minimum when the axion domain wall contributes about $1/3$ of its total mass and does not emit axions. When the annihilation processes starts, the equilibrium state breaks because the mass of the AQN decreases, thus reducing its size. The surrounding domain wall starts to oscillate, generating excitation modes and emitting axions with a typical velocity of $v_{\text{axion}} \approx 0.6c$. Unfortunately, the details of the annihilation process of baryons or nuclei with antiquark matter in the color superconducting phase (2CS or CLF state) are not known. As a simple approximation, in order to estimate the particles generated after the annihilation process and their energy distributions, we supposed that the probability of interaction of the antiquark core with nucleons is similar to the antiproton cross section of nuclear matter. The mechanism through which antiprotons annihilate in interaction with nuclei was explained by Egidy [27], Richard [28], and Amsler and Myhrer [29]. In a standard scenario, a primary annihilation produces mesons, and some of them penetrate the nucleus, giving rise to a variety of other phenomena, including pion production, nucleon emission, internal excitation, etc. Complete and detailed experimental data exist in the classical paper of Chamberlain et al. [30].

The main experimental characteristics of the particles in the final states are listed as follows: (i) A number of pions (as average at rest and in flight) equal to $\langle N_\pi \rangle = 5.36 \pm 0.3$, with average total energy (at rest and in flight) of $\langle E_\pi \rangle = 350 \pm 18 \text{ MeV}/\pi$; (ii) Among these pions, 1.3 and 1.9 interact with the nucleus at rest and in flight, respectively, giving rise to nuclear excitation and nucleon emission; (iii) 0.4 of interacting pions are inelastically scattered, and the effect is a degradation of the primary pion energy to $\langle E_\pi \rangle = 339 \pm 18 \text{ MeV}$; (iv) An average number of 1.6 ± 0.1 of the pions produced in the annihilation interact with the nucleus in which the annihilation occurs, with the effects of nuclear exci-

tation and nucleon emission. The average number of protons emitted per annihilation is $\langle N_B \rangle = 4.1 \pm 0.3$, and the corresponding total average energy release in protons and neutrons is $\langle \Sigma E_B \rangle = 490 \pm 40$ MeV.

In the laboratory frame, from $\pi_0 \rightarrow \gamma + \gamma$, the energies of photons are in the energy range of $0 \leq E_\gamma \leq E_{\pi_0}$ with a flat distribution. From the decay of charged pions, $\pi \rightarrow \mu + \nu$, the energy of muons is $0.58E_\pi \leq E_\mu \leq E_\pi$. Since the annihilation processes occur within nuclei, nuclear effects may alter these results. However, the similarity between values at rest and in flight suggests minimal differences.

If the annihilation takes place in the nucleus, in accordance with the description of Plendl and co-workers [31], the principal steps that are assumed to take place just before, during, and after the intranuclear cascade (INC) caused by annihilation are the following: (a) capture of antimatter structure into high- n atomic orbit; (b) cascade to low- n atomic orbit as intermediate steps from annihilation; (c) mesons K , η , ρ , ω , and π are produced between 2 and 8 with energies of 20 to 600 MeV/ π ; (d) direct emission of kaons and pions from annihilation; and (e) other successive processes, including multi-pion-induced INC of πN , πNN , NN , energetic n , and p from INC coalescence and emission of d , t , ^3He , and ^4He from pre-equilibrium or multifragmentation. The time scale for all these processes is between 0 s (direct annihilation) and $10^{-18} \div 10^{-17}$ s.

Processes initiated in an A $\bar{Q}N$ present critical differences compared with nucleon–antinucleon annihilation. Depending on the parameters, the inside of the A $\bar{Q}N$ exists in a color superconducting phase (CS or CFL) with a gap parameter of $\Delta \approx 100$ MeV, while the outside consists of a free Fermi gas of positrons to maintain neutrality. In the CFL phase, colored quark matter and gluons at high densities can be in excited states. They are strongly interacting quasi-particles, and the energy is ultimately transferred to lower-energy degrees of freedom which, are Nambu–Goldstone (NG) bosons. NG bosons are collective excitations of a diquark condensate. More details from the theoretical point of view and concrete equations for mass calculations and the dispersion relations are provided in the papers of Alford and collaborators [32] and Lawson and Zhitnisky [33]. For these states, peculiarities include an inverted mass spectrum, with kaons being lighter than pions.

In this article, we are interested in determining the energy deposited by an A $\bar{Q}N$ following its annihilation in rocks in order to find a direct detection method using absorbed dose measurements. Zhitnisky [19] and Budker et al. [34] estimated the number of frontal collisions of environmental molecules with an A $\bar{Q}N$ per unit time, the energy rate deposited by A $\bar{Q}Ns$ as a result of annihilation processes, and the energy transfer per unit distance in the material of the environment. Unfortunately, in the absence of relevant experimental results, the energy transfer following the annihilation process from the nuclear state of colored superconductivity to that of normal nuclear matter, along with the kinematic properties of the resulting particles, are not fully understood.

In order to estimate the annihilation probability for the incident protons on the A $\bar{Q}N$ core, it was assumed that the typical cross section is of the order of an antiproton cross section on nuclear matter, and a value of $\sigma \approx 0.4$ b was considered [35–37]. This annihilation process is considered near the surface of the A $\bar{Q}N$, and different estimations of the energies of different particles produced after annihilations are given. In a recent paper, Flambaum et al. [38] introduced a series of constraints in the case of annihilations, considering the absorption of energy after these processes through strong and electromagnetic interactions that prevent weak disintegrations with neutrino emission. The authors estimated that a suppression factor $< 3.3 \times 10^{-4}$ must be considered for the emitted mesons. The numerical results that we present below use these assumptions.

3. Basic Concepts for Detection of A $\bar{Q}Ns$

Because the fluxes of A $\bar{Q}Ns$ are unknown and have not been unambiguously observed so far, the conservative assumption is that interaction rates, if any, are small. Therefore, massive detectors sensitive to these particles and long exposure times are required, or it is necessary to use nonstandard techniques for detection. Large classes of geological minerals

present sensitivity to energies deposited in different interaction processes with projectile particles. An additional requirement is that the signals produced in the form of latent signals be stable for as long as possible, depending on the ambient conditions. For different materials, due to the link between the luminescence process and the deposited energy, this is an excitation process used for dosimetric purposes. The predicted lifetimes [21], for storage at 15 °C are of the order of 10^8 year and decrease exponentially with increasing temperature.

Fluorite (CaF_2) is commercially known as fluorspar. The deposits of fluorite occur in a variety of geologic environments throughout the globe (see for example Figure 1 from reference [39]). Silicate minerals are rock-forming minerals made up of silicate groups. These minerals represent up to approximately 90 percent of Earth's crust. For the present study, SiO_2 is especially important. The U.S. Mineral Resources Data System (MRDS) [40] offers comprehensive maps and precise location data on silicon dioxide (SiO_2) and calcium fluoride (CaF_2) deposits.

Sedimentary quartz (SiO_2), natural calcium fluoride (CaF_2), and feldspars ($x[\text{AlSi}_3\text{O}_8]$ with $x = \text{K, Na, Ca}$) present luminescence properties and are widely distributed in the Earth. Minerals, exposed to different types of radiation since the time of their formation, have accumulated doses of radiation over time in the form of latent signals, which can be extracted by appropriate physical methods. In the case of luminescence signals, the "reading" of this information can be extracted through thermoluminescence (TL) or Optically Stimulated Luminescence (OSL) techniques. Conventionally, TL measurements are conducted by recording light emission in samples during heating. Much more information can be gained by monitoring the details of the emission spectrum during thermoluminescence. TL spectra of minerals exhibit changes as a result of crystal purity, radiation dose, dose rate, and thermal history [41].

If the dose accumulation is proportional to the deposited energy and there are no fading effects, then the read dose is proportional to the total energy. In the case of rare events, in principle, the total integrated dose is the sum of contributions due to the cosmic background or from other sources and singular contributions, with random spatial locations associated with axion antiquark nugget-type events. Different components relevant for the calculation of dose rate for luminescence include cosmic rays from space (protons, heavy ions, electrons, muons, photons, etc.), which decrease with depth; external radiation flux from neighboring grains, such as ^{40}K , ^{232}Th , and ^{238}U chains (including α , β , and γ radiation); and internal radiation, potentially from ^{40}K and other sources.

This background, as paleodose (D_b) [Gy], is calculated as the integrated luminescence [year] multiplied by the dose rate [Gy/year]. If a singular annihilation event of an AQN occurs in a region with mineral deposits of interest (such as feldspars, quartz, calcite, etc.) at a certain depth, an overdose (D_{AQN}) with a certain spatial distribution and approximately spherical symmetry is generated so that

$$D_{\text{AQN}} = D - D_b. \quad (5)$$

4. Numerical Results and Predicted Doses Produced by the Annihilation of AQNs

4.1. Energy Loss of AQNs in Air and Rocks

The energy per unit length produced by annihilation inside an AQN when it travels through the atmosphere or underground can be expressed as follows [34]:

$$-\frac{dE}{dx} = \begin{cases} \approx 10^4 \cdot \kappa \left(\frac{B}{10^{25}}\right)^{2/3} \left(\frac{n_{\text{air}}}{10^{21}\text{cm}^{-3}}\right) \frac{\text{J}}{\text{m}} & \text{for atmosphere,} \\ \approx 10^7 \cdot \kappa \left(\frac{B}{10^{25}}\right)^{2/3} \left(\frac{n_{\text{rock}}}{10^{24}\text{cm}^{-3}}\right) \frac{\text{J}}{\text{m}} & \text{for rocks,} \end{cases} \quad (6)$$

where n_{air} is the total number of nucleons in atoms such that $\rho_{\text{air}} = n_{\text{air}}m_p$; thus, $n_{\text{air}} = 7.7 \times 10^{21} \text{ cm}^{-3}$. n_{rock} is the total number of nucleons in atoms such that $\rho_{\text{rock}} = n_{\text{rock}}m_p$; thus, $n_{\text{rock}} = 1.8 \times 10^{24} \text{ cm}^{-3}$. κ represents a parameter that acknowledges a phenomenon whereby not all matter striking the nugget undergoes annihilation and not all of the energy

released by an annihilation event is fully thermalized within the nuggets. For instance, a portion of the energy is emitted in the form of axions and neutrinos.

Considering $\kappa \approx 1$, the energy released in the atmosphere is ~ 7.7 kJ/m, and the energy released in rocks is ~ 18 MJ/m. Increasing the density of the surrounding material significantly amplifies the released annihilation energy. In the underground case, if one removes the low-energy positrons from the electrosphere, an additional suppression factor of $\xi \sim 10^{-2}$ or even much smaller has to be introduced in the estimation of the energy loss via annihilation processes.

The internal temperature of the an A $\bar{Q}N$ propagating in the Earth's atmosphere can be expressed as follows [42]:

$$T_{\text{atm}} \approx 40 \text{ keV} \cdot \left(\frac{n_{\text{atm}}}{10^{21} \text{ cm}^{-3}} \right)^{4/17} \kappa^{4/17}, \quad (7)$$

The electric charge of the A $\bar{Q}N$ can be written as a function of the temperature (T) as follows [19]:

$$Q \approx \frac{4\pi R^2}{\sqrt{2\pi\alpha}} (m_e T) \frac{T^{1/4}}{m_e} \quad (8)$$

In the case of solids, the temperature is $T \approx (100 - 200)$ keV; thus, the electric charge of the A $\bar{Q}N$ becomes $\approx (7.8 \times 10^8 \div 1.86 \times 10^9)|e|$, and the energy loss via ionization is $\approx 10^{16}$ GeV/cm. The collision of A $\bar{Q}N$ s with dense media such as rocks should release a huge amount of energy on the order of hundreds of MJ/m, equivalent to several kg of TNT, in accordance with Table 1 in Ref. [38].

The rate at which antimatter quark nuggets (A $\bar{Q}N$ s) hit Earth's surface is very low and can be calculated as follows [43]:

$$\varnothing_{\text{AQN}}^{\text{Earth}} = \frac{\langle \dot{N} \rangle}{4\pi R_{\text{Earth}}^2} = 0.4 \times \frac{10^{24}}{\langle B \rangle} \frac{\rho_{\text{DM}}}{0.3 \text{ GeV/cm}^3} \frac{\langle v_{\text{AQN}} \rangle}{220 \text{ km/s}} \left[\frac{1}{\text{km}^2 \text{ year}} \right] \quad (9)$$

This indicates that lighter A $\bar{Q}N$ s tend to have a higher overall flux. Given that the average speed of local dark matter is $\langle v_{\text{AQN}} \rangle$ and the density (ρ_{DM}) is approximately $0.3\text{--}0.4$ GeV/cm³ [44], the estimated flux of A $\bar{Q}N$ s hitting Earth ($\varnothing_{\text{AQN}}^{\text{Earth}}$) is expressed as follows:

$$\varnothing_{\text{AQN}}^{\text{Earth}} = \begin{cases} 2 \times 10^{12} \text{ AQNs/year,} & \text{for } \langle B \rangle = 10^{20}, \\ 2 \times 10^7 \text{ AQNs/year,} & \text{for } \langle B \rangle = 10^{25}. \end{cases} \quad (10)$$

To simulate the expected dose, we used the FLUKA 4-3.4 code [45,46] alongside the Flair graphical interface [47]. FLUKA code can simulate nuclear reactions, produce secondary particles, and model advanced geometries in order to ensure accurate and reliable assessment of the deposited doses in different types of environments. The transport of charged particles is carried out using the Multiple Coulomb scattering algorithm, with an optional single scattering method also available. The electromagnetic physics models in FLUKA describe continuous energy losses of charged particles, energy loss straggling, delta-ray production, and multiple Coulomb scattering.

The spatial distribution of particles produced in \bar{p} annihilation in CaF₂ and SiO₂ is spherically symmetric. Figure 1 represents the dose deposited by e^+ / e^- , p , π^+ / π^- , d , α in one annihilation process in CaF₂ and SiO₂ with respect to the distance from the annihilation point. The difference between the total deposited dose and the contribution of these particles is labeled as "Other particles", i.e., n , μ , t , K , etc. The ratio between the dose deposited by each type of particle and the total dose is represented in Figure 2. It can be seen that the main contributions are from electrons and positrons, along with protons and charged pions.

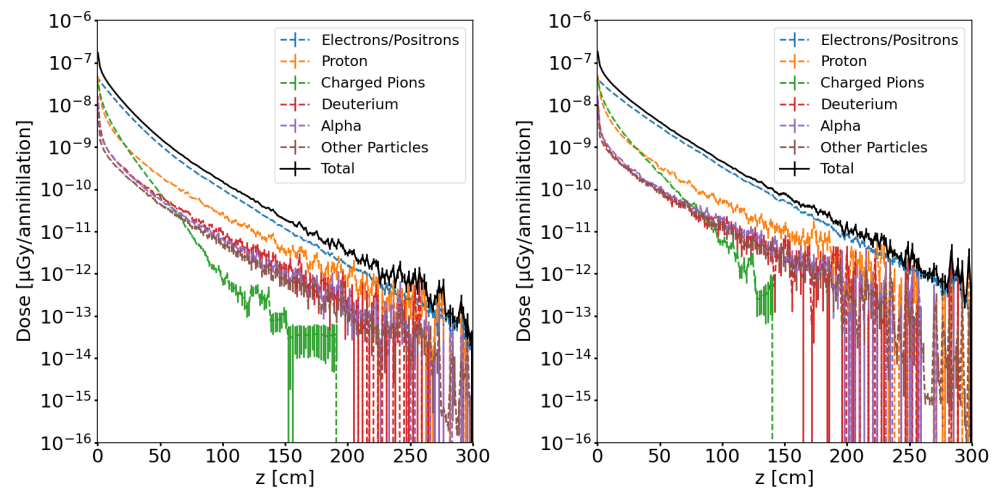


Figure 1. The dose deposited by e^+ / e^- , p , π^+ / π^- , d , α in one annihilation process in CaF_2 (left) and SiO_2 (right) as a function of the distance from the annihilation point. The difference between the total deposited dose and the contribution of these particles is labeled as “Other particles”, i.e., n , μ , τ , K , etc. The suppression of the emission of some particles, particularly pions, was not taken into account.

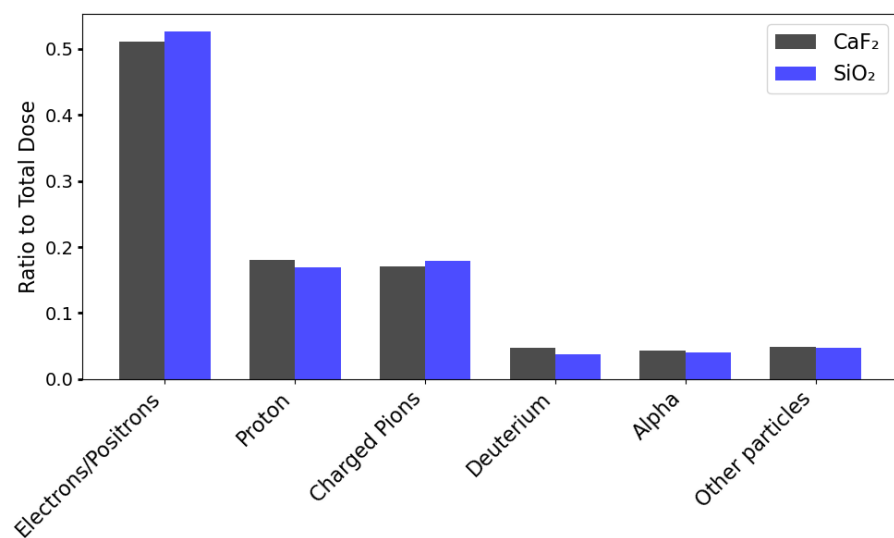


Figure 2. Fraction of dose generated by each type of particle in CaF_2 and SiO_2 for each type of particle produced in the antiproton annihilation event. The main contributions are from electrons and positrons, along with protons and charged pions. The suppression of the emission of some particles, particularly pions, was not taken into account.

A comparison between the total doses generated by particles from a single annihilation process in each medium as a function of the z -axis is shown in Figure 3.

In order to obtain the total deposited dose, these values should be multiplied by the number of annihilation processes. Luminescence dosimetry has a high level of sensitivity, with remarkably low detection limits for radiation doses. The smallest dose recorded using a natural dosimeter with TL technology is $1 \mu\text{Gy}$, achieved with calcium fluoride ($\text{CaF}_2\text{:N}$). In contrast, the Lowest Detectable Dose Limit (LDDL) for sedimentary quartz dosimeters is 1mGy , although in some cases, this limit can be reduced by one order of magnitude [21,48,49].

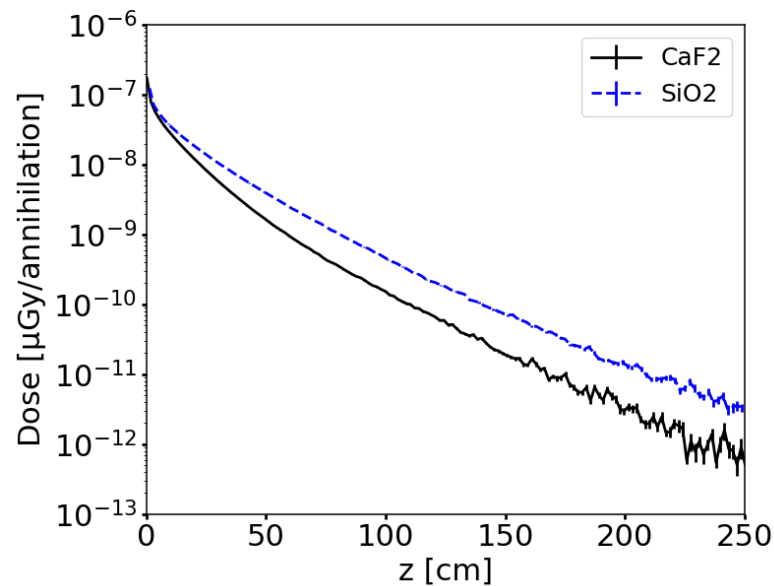


Figure 3. A comparison between the total dose generated by a single antiproton annihilation in CaF_2 and SiO_2 as a function of the z -axis. In order to obtain the total deposited dose, these values should be multiplied by the number of annihilation processes.

Analyzing the energies deposited in the two minerals by all types of particles following the annihilation, we reached the following conclusions: (a) Over 50% of the deposited energy is due to electrons/positrons, over 20% is due to pions, and the remainder is due to other particles. (b) Working under conservative assumptions and including the suppression of the emission of some particles, particularly pions, the doses contributed by electrons/positrons remain unaffected. (c) If we consider only the doses contributed by electrons and positrons, then at a distance of 1 m from the place of annihilation, the obtained value exceeds the lowest detectable dose limit in CaF_2 if the number of annihilated protons is greater than 10^{10} and in SiO_2 if more than 10^{12} annihilations occur.

4.2. Numerical Values for the Contribution of the Radioactive Background to Dose

Cosmic rays interact with the nuclei of atmospheric constituents, producing a cascade of interactions and secondary reaction products that contribute to cosmic ray exposure, which decreases in intensity with depth in the atmosphere from the stratosphere to ground level. The primary types of radiation that originate in outer space and impinge on the top of the Earth's atmosphere consist of 87% protons, 11% α particles, about 1% nuclei with atomic numbers between 4 (beryllium) and 26 (iron), and about 1% electrons of very high energy. They originate outside the solar system, and only a small fraction is normally of solar origin; however, the solar component becomes significant during solar flares, which follow an 11-year cycle. The interactions of the primary particles with atmospheric nuclei produce electrons, γ rays, neutrons, and mesons. At ground level, the dominant component of the cosmic ray field consists of neutrinos and muons, with energy mainly between 1 and 20 GeV [50].

A worldwide contour map of the cosmic-ray dose rates at ground level is available in [51], for a dose-rate interval between 20 and 600 nSv/h (equivalent 0.18 to 5.26 mSv/year). The values are calculated in the frame of the PARMA model coupled with ETOPO2v2 global relief data, which are provided by the National Geophysical Data Center.

In the absence of direct information related to the dose rates produced by abundances of uranium, thorium, potassium, and their descendants in minerals and rocks, we investigate the abundances of these elements in the different classes of materials, predominantly those with low contents of radioactive elements. Most of the information presented here is from Ref. [52]. The abundances of uranium in igneous rocks such as basalts and other mafic or ultramafic rocks fall between 0.001 and 1 ppm, 1–6 ppm in intermediate rocks, 2–50 ppm

in granites and rhyolites, and 0.1–26 ppm in syenites and phonolites. Between sedimentary rocks, shales, clays, and mudrocks, abundances are 1–5 ppm, those in sandstones are sandstones 0.5–4 ppm, and those in limestones and dolomites are <0.1–9 ppm. Metamorphic rocks are characterized by abundances <1–5 ppm. Thorium is a relatively rare element. For basalts and other mafic and ultramafic rocks, limestones, and dolomites, the abundances are in the range of <0.05–3–4 ppm.

Potassium abundances in igneous rocks are the lower in ultramafic rocks (<10 ppm–1%) and basalts and other mafic rocks (1–2)%. In sedimentary rocks, pure gypsum potassium does not exist, and rocks of interest are shales, clays, mudrocks, limestones, and dolomites, with abundances <0.01–7.1%. In order to look for singular events of interactions of A $\bar{Q}N$ with these rocks, first of all, the complete or partial annihilation of the A $\bar{Q}N$ core of the rocks/minerals in which these processes occur must be searched for and be characterized by the lowest abundances of uranium, thorium, and potassium. The doses accumulated from cosmic radiation should be as low as possible, and the temperature of the environment should be constant and as low as possible throughout the year.

5. Summary and Conclusions

This paper investigates the possibility that A $\bar{Q}N$ s, potential exotic particles associated with dark matter, could be detected using natural mineral deposits (CaF₂ and SiO₂) by exploiting TL/OSL techniques. The proposed approach involves identifying regions with excess doses of these materials. Because A $\bar{Q}N$ s are currently hypothetical particles, a series of simplifying hypotheses was considered for their interactions with matter. If the region of interest is characterized by spherical symmetry and has a spatial extension predicted by calculations, it is plausible to attribute these signals to A $\bar{Q}N$ annihilations. Given a background with radioactivity kept as low as possible and a minimum detectable dose limit for TL/OSL in both materials, in accordance with values reported in the literature, A $\bar{Q}N$ s can be detected if at least 10¹⁰ and 10¹² protons annihilate in CaF₂ and SiO₂, respectively.

Author Contributions: Both authors contributed to all parts of this work. All authors have read and agreed to the published version of the manuscript.

Funding: This work was performed with the financial support of Romanian Program PNCDI III, Programme 5, Module 5.2 CERN-RO, under contract no. 04/2022.

Data Availability Statement: Data are contained within the article.

Acknowledgments: We express our deep gratitude to Konstantin Zioutas for inviting and encouraging us to publish this article, as well as for the relevant scientific discussions related to the components of dark matter and its interactions in the universe. His comments and new ideas were extremely stimulating for our work. We also express our gratitude to Ariel Zhitnitsky for his comments on certain aspects of the mechanisms of the interactions of nuggets with matter.

Conflicts of Interest: The authors declare no conflicts of interest.

References

1. Cirelli, M.; Strumia, A.; Zupan, J. Dark Matter. *arXiv* **2024**, arXiv:2406.01705.
2. Du, N.; Force, N.; Khatiwada, R.; Lentz, E.; Ottens, R.; Rosenberg, L.J.; Rybka, G.; Carosi, G.; Woollett, N.; Bowring, D.; et al. Search for Invisible Axion Dark Matter with the Axion Dark Matter Experiment. *Phys. Rev. Lett.* **2018**, *120*, 151301. [[CrossRef](#)]
3. Arik, M.; Aune, S.; Barth, K.; Belov, A.; Borghi, S.; Bräuninger, H.; Cantatore, G.; Carmona, J.M.; Cetin, S.A.; Collar, J.I.; et al. Search for Solar Axions by the CERN Axion Solar Telescope with ³He Buffer Gas: Closing the Hot Dark Matter Gap. *Phys. Rev. Lett.* **2014**, *112*, 091302. [[CrossRef](#)] [[PubMed](#)]
4. Ortiz, M.D.; Gleason, J.; Grote, H.; Hallal, A.; Hartman, M.T.; Hollis, H.; Isleif, K.S.; James, A.; Karan, K.; Kozlowski, T.; et al. Design of the ALPS II Optical System. *arXiv* **2021**, arXiv:2009.14294.
5. Brubaker, B.M.; Zhong, L.; Gurevich, Y.V.; Cahn, S.B.; Lamoreaux, S.K.; Simanovskaia, M.; Root, J.R.; Lewis, S.M.; Al Kenany, S.; Backes, K.M.; et al. First Results from a Microwave Cavity Axion Search at 24 μ eV. *Phys. Rev. Lett.* **2017**, *118*, 061302. [[CrossRef](#)]
6. Lee, C.; MADMAX collaboration. Status of the MADMAX Experiment. In *Microwave Cavities and Detectors for Axion Research: Proceedings of the 3rd International Workshop*; Springer: Berlin/Heidelberg, Germany, 2020; pp. 163–168.

7. Vogel, J.K.; Avignone, F.T.; Cantatore, G.; Carmona, J.M.; Caspi, S.; Cetin, S.A.; Christensen, F.E.; Dael, A.; Dafni, T.; Davenport, M.; et al. IAXO—The International Axion Observatory. *arXiv* **2013**, arXiv:1302.3273.
8. Garcon, A.; Aybas, D.; Blanchard, J.W.; Centers, G.; Figueroa, N.L.; Graham, P.W.; Kimball, D.F.J.; Rajendran, S.; Sendra, M.G.; Sushkov, A.O.; et al. The cosmic axion spin precession experiment (CASPER): A dark-matter search with nuclear magnetic resonance. *Quantum Sci. Technol.* **2017**, *3*, 014008. [[CrossRef](#)]
9. Akerib, D.; Bai, X.; Bedikian, S.; Bernard, E.; Bernstein, A.; Bolozdynya, A.; Bradley, A.; Byram, D.; Cahn, S.; Camp, C.; et al. The Large Underground Xenon (LUX) experiment. *Nucl. Instrum. Methods Phys. Res. Sect. A Accel. Spectrometers Detect. Assoc. Equip.* **2013**, *704*, 111–126. [[CrossRef](#)]
10. Brink, P.L.; Ahmed, Z.; Akerib, D.S.; Bailey, C.N.; Bauer, D.A.; Beaty, J.; Bunker, R.; Burke, S.; Cabrera, B.; Caldwell, D.O.; et al. The Cryogenic Dark Matter Search (CDMS) experiment: Results and prospects. *J. Phys. Conf. Ser.* **2009**, *150*, 012006. [[CrossRef](#)]
11. Collaboration, S.; Albakry, M.F.; Alkhatib, I.; Amaral, D.W.P.; Aralis, T.; Aramaki, T.; Arnquist, I.J.; Langroudy, I.A.; Azadbakht, E.; Banik, S.; et al. Effective Field Theory Analysis of CDMSlite Run 2 Data. *arXiv* **2022**, arXiv:2205.11683.
12. Aprile, E.; Abe, K.; Agostini, F.; Ahmed Maouloud, S.; Althueser, L.; Andrieu, B.; Angelino, E.; Angevaere, J.; Antochi, V.; Antón Martín, D.; et al. First Dark Matter Search with Nuclear Recoils from the XENONnT Experiment. *Phys. Rev. Lett.* **2023**, *131*, 041003. [[CrossRef](#)] [[PubMed](#)]
13. Casaus, J. The AMS-02 experiment on the ISS. *J. Phys. Conf. Ser.* **2009**, *171*, 012045. [[CrossRef](#)]
14. Witten, E. Cosmic Separation of Phases. *Phys. Rev. D* **1984**, *30*, 272–285. [[CrossRef](#)]
15. De Rujula, A.; Glashow, S.L. Nuclearites: A Novel Form of Cosmic Radiation. *Nature* **1984**, *312*, 734–737. [[CrossRef](#)]
16. Zhitnitsky, A.R. ‘Nonbaryonic’ dark matter as baryonic color superconductor. *J. Cosmol. Astropart. Phys.* **2003**, *2003*, 010. [[CrossRef](#)]
17. Singh Sidhu, J.; Scherrer, R.J.; Starkman, G. Antimatter as macroscopic dark matter. *Phys. Lett. B* **2020**, *807*, 135574. [[CrossRef](#)]
18. Oaknin, D.H.; Zhitnitsky, A. Baryon asymmetry, dark matter, and quantum chromodynamics. *Phys. Rev. D* **2005**, *71*, 023519. [[CrossRef](#)]
19. Zhitnitsky, A. Axion quark nuggets. Dark matter and matter–antimatter asymmetry: Theory, observations and future experiments. *Mod. Phys. Lett. A* **2021**, *36*, 2130017. [[CrossRef](#)]
20. Baum, S.; Stengel, P.; Abe, N.; Acevedo, J.F.; Araujo, G.R.; Asahara, Y.; Avignone, F.; Balogh, L.; Baudis, L.; Boukhtouchen, Y.; et al. Mineral detection of neutrinos and dark matter. A whitepaper. *Phys. Dark Universe* **2023**, *41*, 101245. [[CrossRef](#)]
21. Polymeris, G.; Kitis, G.; Liolios, A.; Tsirliganis, N.; Zioutas, K. Minerals as Time-Integrating Luminescence Detectors for setting bounds on dark matter particle characteristics. *Nucl. Instrum. Methods Phys. Res. Sect. A Accel. Spectrometers Detect. Assoc. Equip.* **2006**, *562*, 207–213. [[CrossRef](#)]
22. Lawson, K.; Zhitnitsky, A.R. Quark (Anti) Nugget Dark Matter. *arXiv* **2013**, arXiv:1305.6318.
23. Lazanu, I.; Parvu, M. Exploring the detection of AQNs in large liquid detectors. *J. Cosmol. Astropart. Phys.* **2024**, *2024*, 014. [[CrossRef](#)]
24. Gorham, P.W.; Rotter, B.J. Stringent neutrino flux constraints on antiquark nugget dark matter. *Phys. Rev. D* **2017**, *95*, 103002. [[CrossRef](#)]
25. Forbes, M.M.; Zhitnitsky, A.R. WMAP Haze: Directly Observing Dark Matter? *Phys. Rev. D* **2008**, *78*, 083505. [[CrossRef](#)]
26. Toolbox, E. Standard Atmosphere. Available online: https://www.engineeringtoolbox.com/standard-atmosphere-d_604.html (accessed on 20 May 2024).
27. Von Egidy, T. Interaction and Annihilation of Anti-protons and Nuclei. *Nature* **1987**, *328*, 773–778. [[CrossRef](#)]
28. Richard, J.M. Antiproton physics. *Front. Phys.* **2020**, *8*, 6. [[CrossRef](#)]
29. Amsler, C.; Myhrer, F. Low energy antiproton physics. *Annu. Rev. Nucl. Part. Sci.* **1991**, *41*, 219–267. [[CrossRef](#)]
30. Chamberlain, O.; Goldhaber, G.; Jauneau, L.; Kalogeropoulos, T.; Segrè, E.; Silberberg, R. Antiproton-Nucleon Annihilation Process. II. *Phys. Rev.* **1959**, *113*, 1615–1634. [[CrossRef](#)]
31. Plendl, H.S.; Daniel, H.; von Egidy, T.; Haninger, T.; Hartmann, F.S.; Hofmann, P.; Kim, Y.S.; Machner, H.; Riepe, G.; Jastrzebski, J.; et al. Antiproton-nucleus annihilation at rest. *Phys. Scr.* **1993**, *48*, 160. [[CrossRef](#)]
32. Alford, M.G.; Schmitt, A.; Rajagopal, K.; Schäfer, T. Color superconductivity in dense quark matter. *Rev. Mod. Phys.* **2008**, *80*, 1455–1515. [[CrossRef](#)]
33. Lawson, K.; Zhitnitsky, A.R. Solar neutrino spectrum of quark nugget dark matter. *Phys. Rev. D* **2017**, *95*, 063521. [[CrossRef](#)]
34. Budker, D.; Flambaum, V.V.; Zhitnitsky, A. Infrasonic, Acoustic and Seismic Waves Produced by the Axion Quark Nuggets. *Symmetry* **2022**, *14*, 459. [[CrossRef](#)]
35. Flambaum, V.; Samsonov, I. Radiation from matter-antimatter annihilation in the quark nugget model of dark matter. *Phys. Rev. D* **2021**, *104*, 063042. [[CrossRef](#)]
36. Flambaum, V.V.; Samsonov, I.B. Thermal and annihilation radiation in the quark nugget model of dark matter. *Phys. Rev. D* **2022**, *105*, 123011. [[CrossRef](#)]
37. Flambaum, V.V.; Samsonov, I.B. Radiation from cold molecular clouds and Sun chromosphere produced by antiquark nugget dark matter. *Phys. Rev. D* **2022**, *106*, 023006. [[CrossRef](#)]
38. Flambaum, V.V.; Samsonov, I.B.; Vong, G.K. Manifestation of antiquark nuggets in collisions with the Earth. *arXiv* **2024**, arXiv:2405.17775.

39. Magotra, R.; Namga, S.; Singh, P.; Arora, N.; Srivastava, P. A new classification scheme of fluorite deposits. *Int. J. Geosci.* **2017**, *8*, 599–610. [[CrossRef](#)]
40. U.S. Geological Survey. Mineral Resources Data System (MRDS)—Map by Commodity. Available online: <https://mrdata.usgs.gov/mrds/map-commodity.html> (accessed on 11 June 2024).
41. Rendell, H.; Khanlary, M.R.; Townsend, P.; Calderón, T.; Luff, B. Thermoluminescence spectra of minerals. *Mineral. Mag.* **1993**, *57*, 217–222. [[CrossRef](#)]
42. Zhitnitsky, A. Mysterious anomalies in Earth’s atmosphere and strongly interacting Dark Matter. *arXiv* **2024**, arXiv:2405.04635.
43. Liang, X.; Mead, A.; Siddiqui, M.S.R.; Van Waerbeke, L.; Zhitnitsky, A. Axion Quark Nugget Dark Matter: Time Modulations and Amplifications. *Phys. Rev. D* **2020**, *101*, 043512. [[CrossRef](#)]
44. de Salas, P.F.; Malhan, K.; Freese, K.; Hattori, K.; Valluri, M. On the estimation of the Local Dark Matter Density using the rotation curve of the Milky Way. *JCAP* **2019**, *10*, 037. [[CrossRef](#)]
45. Ahdida, C.; Bozzato, D.; Calzolari, D.; Cerutti, F.; Charitonidis, N.; Cimmino, A.; Coronetti, A.; D’Alessandro, G.; Donadon Servelle, A.; Esposito, L.; et al. New capabilities of the FLUKA multi-purpose code. *Front. Phys.* **2022**, *9*, 788253. [[CrossRef](#)]
46. Battistoni, G.; Boehlen, T.; Cerutti, F.; Chin, P.W.; Esposito, L.S.; Fassò, A.; Ferrari, A.; Lechner, A.; Empl, A.; Mairani, A.; et al. Overview of the FLUKA code. *Ann. Nucl. Energy* **2015**, *82*, 10–18. [[CrossRef](#)]
47. Vlachoudis, V. FLAIR: A powerful but user friendly graphical interface for FLUKA. In Proceedings of the International Conference on Mathematics, Computational Methods & Reactor Physics (M&C 2009), Saratoga Springs, New York, NY, USA, 3–7 May 2009; Volume 176.
48. McKeever, S.W.; Moscovitch, M.; Townsend, P.D. *Thermoluminescence Dosimetry Materials: Properties and Uses*. Available online: <https://www.osti.gov/etdeweb/biblio/480679> (accessed on 20 May 2024).
49. Aitken, M. *An Introduction to Optical Dating*; Oxford University Press: New York, NY, USA, 1998.
50. Cinelli, G.; Gruber, V.; De Felice, L.; Bossew, P.; Hernandez-Ceballos, M.A.; Tollefsen, T.; Mundigl, S.; De Cort, M. European annual cosmic-ray dose: Estimation of population exposure. *J. Maps* **2017**, *13*, 812–821. [[CrossRef](#)]
51. Japan Atomic Energy Agency. Exposure Dose Map. Available online: <https://phits.jaea.go.jp/expacs/dosemap-eng.htm> (accessed on 20 May 2024).
52. MediaWiki. OR/17/001 The Distribution of Natural Radioactivity in Rocks. Available online: http://earthwise.bgs.ac.uk/index.php?title=OR/17/001_The_distribution_of_natural_radioactivity_in_rocks&oldid=44337 (accessed on 20 May 2024).

Disclaimer/Publisher’s Note: The statements, opinions and data contained in all publications are solely those of the individual author(s) and contributor(s) and not of MDPI and/or the editor(s). MDPI and/or the editor(s) disclaim responsibility for any injury to people or property resulting from any ideas, methods, instructions or products referred to in the content.